



Evolution of critical buckling conditions in imperfect bilayer shells through residual swelling

Cite this: DOI: 10.1039/c9sm00901a

Anna Lee,  ^{†a} Dong Yan, ^a Matteo Pezzulla, ^a Douglas P. Holmes  ^b and Pedro M. Reis  ^{*a}

We propose and investigate a minimal mechanism that makes use of differential swelling to modify the critical buckling conditions of elastic bilayer shells, as measured by the knockdown factor. Our shells contain an engineered defect at the north pole and are made of two layers of different crosslinked polymers that exchange free molecular chains. Depending on the size of the defect and the extent of swelling, we can observe either a decreasing or increasing knockdown factor. FEM simulations are performed using a reduced model for the swelling process to aid us in rationalizing the underlying mechanism, providing a qualitative agreement with experiments. We believe that the working principle of our mechanism can be extended to bimetallic shells undergoing variations in temperature and to shells made of pH-responsive gels, where the change in knockdown factor could be changed dynamically.

Received 3rd May 2019,
 Accepted 28th June 2019

DOI: 10.1039/c9sm00901a

rsc.li/soft-matter-journal

1 Introduction

From colloidal capsules at the microscale to meter-sized pressure vessels, the buckling of thin shells is observed across a wide variety of length scales and has been challenging scientists and engineers for more than a century.^{1–3} Shell buckling originally was of interest primarily to structural engineers, within the realm of the design and analysis of thin-walled mechanical systems. However, in the last decades, it has become apparent that the buckling of shell structures is also relevant at much smaller scales, both in the living world and in technological settings, with examples, to name just a few, ranging from the Venus flytrap,⁴ to pollen grains,⁵ red blood cells,⁶ and colloidal capsules.⁷

The catastrophic (subcritical) nature of shell buckling has made it an iconic example of an elastic instability; when the difference between the outer and the inner pressure of a shell is increased above a critical value, the shell collapses and loses its load-carrying capacity.² As such, determining the critical buckling conditions of a shell is of extreme importance in the design and prevention against failure. Still, this task has proven to be nontrivial since the catastrophic nature of the instability translates into a high imperfection sensitivity: typically, shells

buckle at significantly lower loads than those suggested by classic theories, in an unpredictable way.⁸ These imperfections can be either due to variations of the geometry or material properties, or both, and can arise either during the fabrication or over the lifetime of the structure. Consequently, it took nearly four decades to reconcile experimental results with the theoretical prediction for the buckling pressure first derived by Zoelly.¹ As a result of the high imperfection sensitivity and to aid in designing and characterizing shell structures, engineers have defined the knockdown factor, κ_d , as the ratio between the maximum experimental load sustained by the shell before buckling and the classic theoretical prediction.⁹ For thin shell structures, κ_d can be as low as 0.2. Rationalizing the factors that dictate κ_d has been a major challenge in engineering mechanics throughout the 20th century¹⁰ and, with the lack of formal predictive frameworks, the practical design of shell structures is mostly limited to empirical guidelines.¹¹

Recently, Lee *et al.*¹² proposed a rapid and simple fabrication technique to manufacture thin shells based on the coating of hemispherical molds with a polymer solution, which eventually cures to produce an elastic shell with nearly uniform thickness. Thin shells produced this way have knockdown factors of up to $\kappa_d \approx 0.9$.¹³ However, even though fabrication techniques can be improved to reduce the number and the size of imperfections, the inherently subcritical nature of shell buckling represents a strong limitation towards the strengthening of shells by merely improving their fabrication. Moreover, as buckling can also be a means towards functionality as in the lock and key mechanism for colloids⁷ or in microswimmers,¹⁴ shells would benefit from being dynamically strengthened or

^a Flexible Structures Laboratory, Institute of Mechanical Engineering, École Polytechnique Fédérale de Lausanne, 1015 Lausanne, Switzerland.

E-mail: pedro.reis@epfl.ch

^b Department of Mechanical Engineering, Boston University, Boston, Massachusetts 02215, USA

[†] Current address: Department of Mechanical Engineering, Pohang University of Science and Technology, Pohang, Gyeongbuk 37673, Korea.

even weakened, depending on their task. While there are some strategies to strengthen shells, such as introducing ribs¹⁵ or fibers,^{16,17} they are tailored primarily to large-scale systems where the introduction of ribs or fibers can be more readily accomplished than at the microscale. Still, some small-scale examples of reinforced shells do exist, such as fiber-reinforced micro-capsules¹⁷ and pollen grains.⁵ The latter have a complex composite structure where the outer layer (known as the exine) is significantly stiffer than the inner layer. These techniques rely on the introduction of stiffening parts in the shells and cannot be extended to weaken or strengthen the shell dynamically.

Here, we introduce and investigate a minimal mechanism to modify the buckling strength of shell structures, making use of differential swelling in a bilayer polymeric structure. The simplicity of our system contrasts with the design strategies mentioned above, which require adding manufacturing complexity to the structure, whereas our mechanism relies solely on a swelling stimulus. In our prototypical example, the shell comprises two layers of different silicone elastomers that undergo differential swelling from residual, uncrosslinked polymer chains after curing when in contact.¹⁸ The sign of the natural curvature induced by residual swelling depends on the relative position of the swelling *versus* the shrinking layers (*i.e.*, which one is on the outside),^{18,19} and we observed marked differences in both the time series of the buckling pressure and its steady-state value. In a region of parameter space, we find that the buckling strength of the bilayer shell can increase or decrease. This problem is analogous to the buckling of bimetallic shells,^{20–25} where the structure can buckle due to a combination of uniform temperature change and applied external pressure. Given that, in practice, no shell is perfect, we decide to study the effect of residual swelling on shells containing a single well-defined engineered defect at the north pole.¹³ Our goal is to investigate whether this geometric imperfection could potentially be either repaired or aggravated, depending on the original shape of the imperfection, as well as on the natural curvature that evolves due to differential swelling.

In the fabrication of our experimental samples, we use two vinylpolysiloxane (VPS) polymer liquids (VPS-32 and VPS-8, Zhermack), which have been shown to undergo differential swelling when in contact after they are fully cured. This process, known as residual swelling, involves residual, uncrosslinked polymer chains that diffuse from one polymer to the other, across their interface.^{19,26} Fig. 1(a and b) presents a schematic of this diffusion process. During curing, polymerization leaves many uncrosslinked free chains in VPS-8 but much fewer in VPS-32. This concentration gradient of free polymer chains causes a net flux of these free chains into the VPS-32 layer (Fig. 1(a)). The associated mass diffusion results in a variation of the volume of each layer (Fig. 1(b)), which, together with geometric confinement, can lead to the build-up of residual stresses that deform the bilayer structure. The two types of bilayer shells are illustrated in Fig. 1(c and d), where the order of the layers is changed in order to change the sign of the

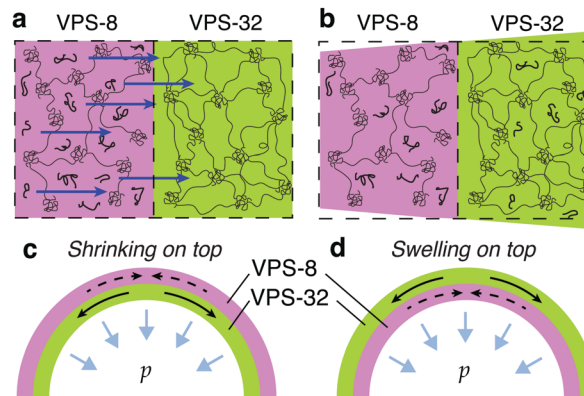


Fig. 1 A schematic of differential swelling in a polymer bilayer and schematics of two types of bilayer shells. (a) Free chains diffuse from VPS-8 (pink) to VPS-32 (green) driven by a concentration gradient. (b) The volume of VPS-8 decreases while the volume of VPS-32 increases as a result of differential swelling. (c) The shrinking layer on top shell consists of VPS-8 (softer and shrinking) outer and VPS-32 (stiffer and swelling) inner layers. (d) The swelling layer on top shell consists of VPS-32 outer and VPS-8 inner layers. Solid arrows correspond to swelling and dashed arrows correspond to shrinking.

natural curvature. From now on, we will refer to the shrinking layer on top shell and the swelling layer on top shell, to indicate the configurations in Fig. 1(c) and (d), respectively.

Our paper is structured as follows. We start by describing the experimental protocols to fabricate hemispherical bilayer shells, measure the buckling pressure, and characterize the deformed shapes of the shells. We then investigate how differential swelling and the initial geometric imperfection change the time-evolution of the knockdown factor. To aid us in rationalizing the underlying mechanism, we conduct Finite Element Method (FEM) simulations to first predict the buckling pressure of the shells using their experimentally measured deformed shape, and then perform a parametric study to investigate the influence of thickness variations, natural curvature, and defect amplitude. We conclude by summarizing our findings and providing an outlook on possible future research.

2 Experimental methods

To characterize the buckling load of elastic shells, we first need to measure their elastic properties, such as Young's modulus and bending stiffness. Most importantly, as our shells are made of two layers of different elastomers that are undergoing differential swelling, we have to characterize the mechanical properties of the structure over time; *i.e.*, as the swelling takes place. To do so, we fabricate an originally flat bilayer beam, which exactly replicates the structure of the shell through its thickness, in terms of both polymers and dimensions. We then study the bending of the beam over time, so as to characterize the swelling in terms of time scale and maximum natural curvature.¹⁹ In Appendix A, we provide the details of this characterization and show that the elastic properties (Young's modulus and bending stiffness) of the bilayer beam remain constant throughout.

We turn to investigate the time dependence of the shape and the buckling strength of bilayer shells made out of both VPS-8 and VPS-32. We will start by describing the protocol that we used to fabricate our bilayer shells, then characterize their shape and, finally, measure their buckling pressure as a function of time.

2.1 Fabrication of hemispherical bilayer shells

We engineer a defect in the shells in order to be able to quantify the effect of differential swelling on the shape of the defect and, consequently, its effect on the critical buckling pressure of the shell (knockdown factor). Note that without a seeded defect that is more dominant than the uncontrollable small imperfections that are intrinsic to the manufacturing process, the experimentally measured knockdown factor cannot be predicted by FEM (see Section 4). Moreover, uncontrollable imperfections could be either repaired or aggravated as a result of the varying natural curvature due to differential swelling (more on this below) and would have unpredictable effects on the measured knockdown factor. We shall show that, by including an engineered defect (a localized deviation from a perfect hemispherical shape), we will be able to quantitatively investigate how differential swelling affects this geometrical defect, thereby dictating the knockdown factor.¹³

We used the thick polydimethylsiloxane (PDMS) molds described in Appendix B to fabricate bilayer shells made out of VPS-8 and VPS-32. The manufactured shell can have the shrinking layer (VPS-8) on top (Fig. 2(b)) or the swelling layer (VPS-32) on top (Fig. 2(c)), depending on the order of coating of each polymeric liquid during the fabrication process. In Fig. 2(a), we illustrate the protocol we developed to fabricate our bilayer hemispherical shells, ensuring clamped boundary conditions at their equator. First, one of the VPS solutions was poured onto the concave underside of the PDMS mold and it was turned upside down to drain the excess polymer and produce a thin lubrication film.¹² The curing time scale of the VPS polymers is approximately 10 min,¹² and both VPS-32 and VPS-8 are fully cured after 20 min. After the first layer of VPS cured, the other VPS solution (VPS-32 or VPS-8, respectively) was poured and drained to produce the second inner layer. During the coating of both VPS layers, small pendant droplets formed at the equatorial rim of the mold, as illustrated in Fig. 2(a). Once the second layer of VPS solution cured, the excess polymer on the bottom surface of the mold was cut out using a scalpel. We enforced that each layer has the same thickness, $h_1 = h_2 = 0.3$ mm, by using the technique presented in Lee *et al.*,¹² and delaying the pouring time $\tau_w = 200$ s for VPS-8 and 260 s for VPS-32, from the moment of preparation of the VPS liquid.

After the fabrication of the bulk of the bilayer shell, we then added a circular plate at its base (equator) in order to close the shell and impose a clamped boundary (otherwise the shell would undergo large deformations due to swelling, and break rotational symmetry¹⁸). To set these boundary conditions, we poured a mixture of VPS-8 and VPS-32 with a ratio 1 : 1 onto the acrylic plate and covered the puddle of this mixture with the

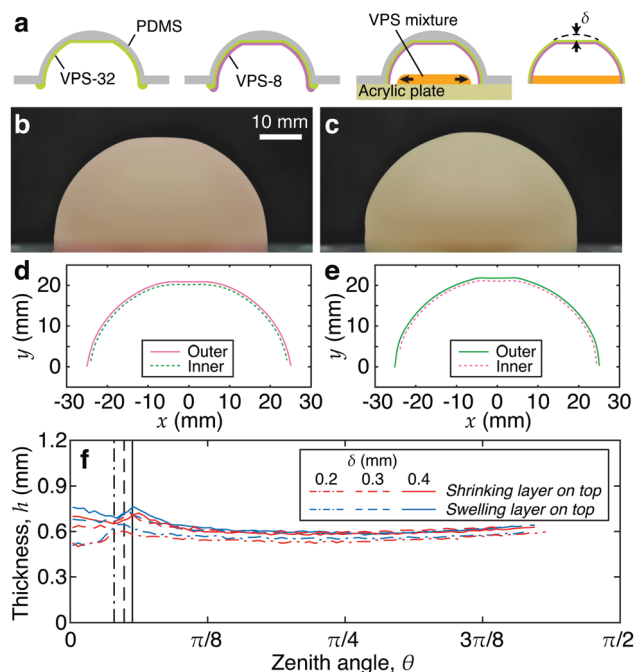


Fig. 2 (a) Fabrication process of a hemispherical bilayer shell that has a flat defect of amplitude δ . Photographs of shells with (b) the shrinking layer (VPS-8) on top and (c) the swelling layer (VPS-32) on top. Profiles of the outer surface (solid line) and the inner surface (dashed line) of the (d) shrinking layer on top and (e) swelling layer on top shells. (f) Thickness profiles as a function of the zenith angle, θ , of the shrinking layer on top and the swelling layer on top shells.

shell. The puddle of VPS mixture gradually spread until the leading edge met the shell at its equator, which, upon curing, formed a band with a thickness of 3.1 ± 0.5 mm, which ensured the clamped boundary condition at the equator. For this base plate of the shell, we used a VPS-8 and VPS-32 mixture to minimize the effect that the base plate had on the differential swelling of the bilayer shell. Had we used pure VPS-8 or VPS-32 as the material of the base plate, we would have observed significant diffusion between the shell and the base plate. We measured and compared the natural curvature of an open bilayer shell (without the base plate) and a closed one (with the base plate) and found no difference between them, which reveals that the base plate did not affect the differential swelling of the shell. Finally, the bilayer shell closed with the plate at its equator was peeled from the PDMS shell, and a hole was made at the center of the bottom plate.

We define $t = 0$ as the instant of time when the second layer of the shell is poured onto the first, already cured, shell. The first buckling pressure measurement was taken at $t \approx 30$ min because the polymerization of the shell and the thicker band at the equator, together with the preparation to measure the buckling pressure, required $t \approx 30$ min. We fabricated a set of bilayer shells with a systematic variation of the amplitude of the defect, $\delta = \{0, 0.1, 0.15, 0.2, 0.25, 0.3, 0.35, 0.4, 0.45, 0.5\}$ mm, where VPS-32 could be on top of VPS-8, or the reverse. For all samples, the radius of the shell was $R = 25.1$ mm, and the thickness was $h = 0.6$ mm, such that the radius to thickness

ratio was $\eta \equiv R/h = 42$. This value of η satisfies the condition for a thin shell $\eta \geq 20$, as described in Ventsel and Krauthammer,²⁷ but our shell is still much thicker than the shells used in other shell buckling experiments ($\eta > 70$). However, if the thickness of the shell were decreased, the diffusion time scale would decrease steeply since $T \sim h^2$ as discussed also in Pezzulla *et al.*,²⁶ so that it would become difficult to investigate the time-evolution of the knockdown factor, which is addressed in the next section.

2.2 Protocol to measure the critical buckling pressure of bilayer shells

We recall that the knockdown factor κ_d is defined as the maximum experimentally measured pressure, p_{\max} , which the shell can withstand, normalized by the classical buckling pressure, p_c , for a perfect shell. The critical buckling pressure for a perfect bilayer shell, p_c , was obtained by FEM with linear buckling analysis. In the FEM simulations, the bilayer shells had the same parameters as the shells used in our experiments, but the mass diffusion of free chains was not considered. The shell has a radius $R = 25.1$ mm, and the thickness of each layer was forced to be constant $h_1 = h_2 = 0.3$ mm. The Young's moduli of each layer were also assumed to be constant over time (Section 4), which is consistent with our experimental measurements.

The shell was mounted onto an acrylic plate with a hole at its center, and connected to both a syringe pump (NE-1000, New Era Pump Systems, Inc.) and a pressure sensor (MPXV7002, NXP semiconductors). The air inside the shell was extracted at an imposed constant flow rate of 0.6 ml min^{-1} for 1 min, and then injected back into the shell with a constant flow rate of 0.6 ml min^{-1} for 1 min. For each shell, we repeated these measurements as a function of time to obtain time-series of the critical buckling pressure. This air extraction–injection process was repeated automatically every five minutes by programming the syringe pump. The internal pressure was monitored at an acquisition rate of 1 Hz using the pressure sensor. During the air extraction period, the inner volume of the shell decreased, until the shell buckled, at which point a minimum value of the internal pressure and its time were recorded. Beyond this point, the shell deformed further, decreasing its volume, until the end of air extraction. During the next air injection cycle, the deflection was reduced, and finally the shell returned to the original shape at the end of the air injection. After a 3 min pause, the air extraction–injection process was repeated, so the time-step of the measuring process is 5 min.

2.3 Characterization of the final shape of the bilayer shells through X-ray tomography

As shown in Section B of the appendix, differential swelling of a bilayer beam causes its natural curvature to evolve. For the case of bilayer shells, this swelling is also expected to modify the shape of an existing defect. Consequently, a change in the geometry of the imperfection, albeit small, can have a large effect on the knockdown factor. Thus, prior to presenting the results on the knockdown factor (Section 3), we shall first quantify the shape of our bilayer shells in their final steady state, which, eventually, will enable us to evaluate how the

deformation of the defect relates to the variation of the knockdown factor. The shape profiles reported next will also be used in the FEM simulations (Section 4).

X-ray computed tomography (CT), together with digital image processing, was employed to obtain three-dimensional (3D) data on the full geometry of the bilayer shells. Specifically, we focused on obtaining data on the outer and inner surfaces, from which we could readily compute the thickness profile of the shells. We found that the shape of the shell remained axisymmetric throughout the differential swelling process. From the outer/inner surface data, we extracted curves along three meridians (at different azimuthal angles) and averaged them to obtain the axisymmetric shell shape, as well as its thickness profile. This nondestructive technique prevented us from having to cut the shell for inspection. The scanning resolution was $26 \mu\text{m}$ (voxel size), and each scan took approximately 1 h. As such, we could not obtain time-dependent data from the X-ray CT and, instead, we only quantified shells in the steady state (at least after 1 day past fabrication), once the shape had ceased to evolve due to saturation of differential swelling.

In Fig. 2(b and c) we show photographs of the steady state of two representative bilayer shells, one with the shrinking layer on top (Fig. 2(b)) and one with the swelling layer on top (Fig. 2(c)). Both of these shells were fabricated to contain a defect with an initial amplitude of $\delta = 0.4$ mm, corresponding to $\delta/h = 0.66$. In Fig. 2(d and e), we plot the corresponding profiles of their outer and inner surfaces (solid and dashed lines, respectively). The shrinking layer on top shell has a large and smooth defect; see Fig. 2(b and d). On the other hand, the swelling layer on top shell has a smaller and sharper defect; see Fig. 2(c and e). For other shells with different values of the initial defect amplitude, we found that the steady-state shape near the defect varies accordingly but the shape of the rest of the shell remains nearly the same.

Beyond the outer shape of the defect (which could have alternatively been obtained in an easier way using a contactless profilometer), any potential spatial variation of the shell thickness (the quantification of which can only be obtained through tomography) must also be treated as an imperfection. If present, such thickness variations are important as they would likely contribute significantly to affecting the buckling behavior and must, therefore, be quantified. We expect the thickness profile of our imperfect shells to be nonuniform in the vicinity of the defect due to fabrication details associated with the viscous flow of the polymer suspension coating the surface of the mold, which precedes curing. Our shells could exhibit non-uniform thickness due to two effects. First, under the flat part of the mold (which shapes the initial shape of the defect), the Rayleigh–Taylor instability²⁸ can occur when the defect is large, which would induce a localized increase of the thickness. Second, it is known that the thickness of a liquid film flowing over a complex surface increases at a concave corner.^{29,30} In our shells, this effect could translate into the VPS film having a maximum thickness along the circular edge of the defect. We examine these two possibilities by extracting the thickness profile from our X-ray CT scans.

In Fig. 2(f), we plot the final (steady state) thickness profiles for a set of shells, as a function of the zenith angle θ . As representative cases, we selected shells containing a defect with the following initial amplitudes, $\delta = \{0.2, 0.3, 0.4\}$ mm (dashed-dotted, dashed, and solid lines, respectively), the three of which could either have the shrinking layer on top (red lines) or the swelling layer on top (blue lines). The shrinking layer on top shell and swelling layer on top shell have nearly the same thickness profiles, indicating that the non-uniformity results from the fabrication procedure (viscous coating), rather than from differential swelling. The thickness at the pole was measured to be $h_{\theta=0} = \{0.51, 0.66, 0.73\} \pm 0.03$ mm, for the shells with $\delta = \{0.2, 0.3, 0.4\}$ mm, respectively. The larger values of $h_{\theta=0}$ are obtained for the shells with the larger values of δ , which is compatible with the accumulation of VPS at the pole due to Rayleigh–Taylor effects. Beyond the pole, another maximum of thickness occurs near the edge of the defect (black vertical lines in Fig. 2(f)), with values of $h_{\beta} = \{0.64, 0.73, 0.75\} \pm 0.02$ mm for $\delta = \{0.2, 0.3, 0.4\}$ mm, respectively. The existence of this second maximum is consistent with the mechanism mentioned above for the increase of the thickness of a film near a concave corner (which is the case at the edge of the defect). Away from the defect, the thickness decreases to 0.6 mm in the rest of the shell, for all the cases evaluated.

The non-uniformity of the thickness reported above will need to be included in the FEM simulations presented in Section 4, and must also be considered when interpreting the experimental results on the knockdown factor, which we present next.

3 Experimental results on the time-varying knockdown factors

We proceed by making use of the experimental protocols presented above to quantify how the critical buckling pressure, and hence the knockdown factor, of our bilayer shells evolves over time due to differential swelling. We shall also compare the knockdown factors of the shrinking layer on top and swelling layer on top shells, and systematically explore how the evolution of κ_d is affected by the amplitude of the defect. In Fig. 3, we plot time series for $\kappa_d(t)$, for the two cases of the shrinking layer on top shells (Fig. 3(a)) and swelling layer on top shells (Fig. 3(b)).

The experimental results reported in Fig. 3 clearly show that the shrinking layer on top shells become weaker with time, that is with a positive increasing natural curvature, except for some noise when the defects are small ($\delta/h < 0.3$) since other imperfections coming from the fabrication procedure might have a comparable influence. The swelling layer on top shells, that is shells with a negative decreasing natural curvature, become weaker over time for small defects ($\delta/h < 0.16$), but heal and get stronger for larger defects, resulting in an increasing knockdown factor over time. Specifically, when the defect amplitude is small ($\delta = \{0, 0.1, 0.2\}$ mm), the knockdown factor of the shrinking layer on top (Fig. 3(a)) shells slightly decreases

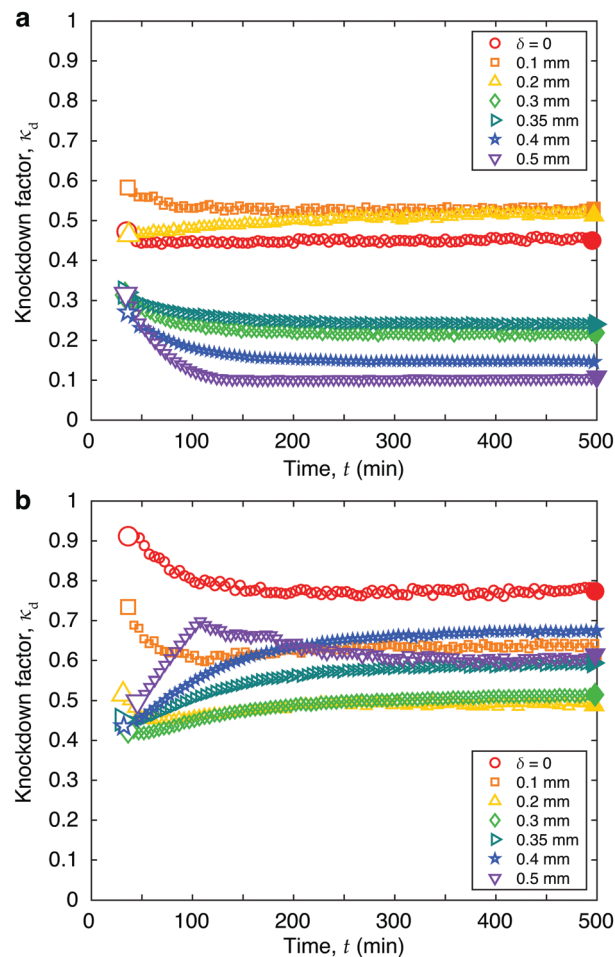


Fig. 3 Knockdown factor versus time. Experimental results of the knockdown factor of the (a) shrinking layer on top shells and (b) swelling layer on top shells with $R = 25.1$ mm and $h = 0.6$ mm. The amplitude of the flat defect is varied, $\delta = \{0, 0.1, 0.2, 0.3, 0.35, 0.4, 0.5\}$ mm.

from $\kappa_d = 0.53 \pm 0.06$ to $\kappa_d = 0.49 \pm 0.04$, a decrease of about 8%. With larger defects ($\delta = \{0.3, 0.35, 0.4, 0.5\}$ mm), both the initial and steady-state knockdown factor are lowered. The knockdown factor decreases from $\kappa_d = 0.30 \pm 0.03$ to $\kappa_d = 0.17 \pm 0.07$ ($\approx 43\%$).

For the swelling layer on top shells (Fig. 3(b)), when the defect is small ($\delta = \{0, 0.1\}$ mm), the knockdown factor decreases non-monotonically by 16% and 12%, respectively. For larger defects, the shell gets stronger, increasing its knockdown factor, for example, by 19% when $\delta = 0.3$ mm and by 55% when $\delta = 0.4$ mm. Some non-monotonic behavior is observed for shells with even larger defects. For example, for the case with $\delta = 0.5$ mm, buckling first occurs at the defect, and then, once κ_d reaches the maximum value, additional buckling events occur close to the equator, meaning that the seeded defect is not the most critical imperfection. This is because the large thickness at the center compensates the effect of the geometric imperfection. Moreover, when the defect is small ($\delta = \{0, 0.1\}$ mm), the other uncontrollable imperfections can have more significant effects on shell buckling.

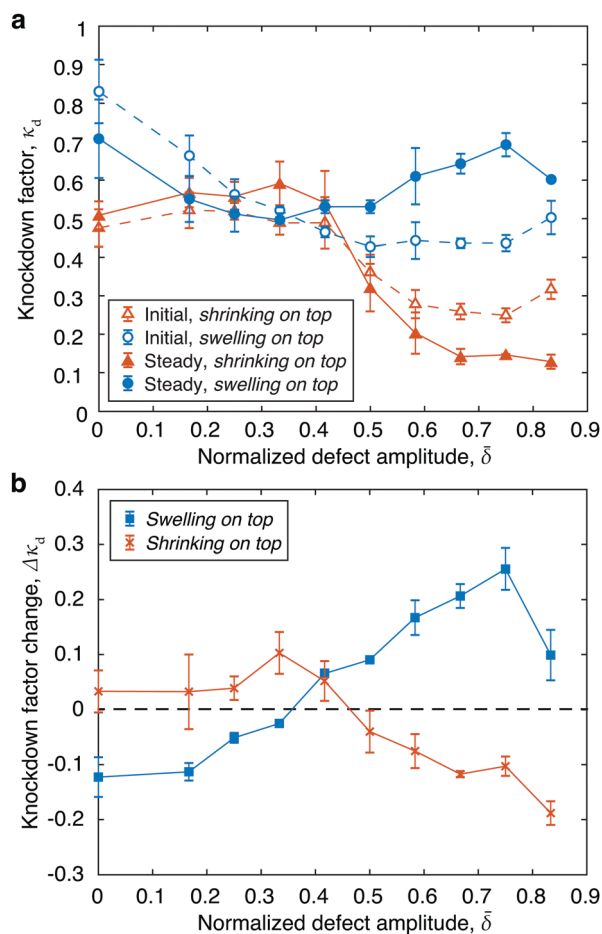


Fig. 4 (a) Knockdown factor versus normalized defect amplitude in the initial state (empty symbols) and in the steady state (solid symbols). (b) Knockdown factor change from the initial to the steady-state as a function of normalized defect amplitude.

In Fig. 4(a), we plot the initial (open symbols) and the final (solid symbols) values of the knockdown factor, κ_d , as a function of the normalized defect amplitude, $\bar{\delta} = \delta/h$, for both the swelling layer on top shells (blue circles) and the shrinking layer on top shells (orange triangles). These open and solid symbols correspond to the large open and solid symbols in Fig. 3, respectively. The time-series in Fig. 3 is a subset of all the data, and here Fig. 4 shows all the data with error bars. With the same initial amplitude of the defect, the swelling layer on top shells are generally stronger than the shrinking layer on top shells. The error bars of the data in this figure correspond to the standard deviation of three buckling pressure measurements, with three different shells.

For the swelling layer on top shells in the initial state (empty circles), the knockdown factor continuously decreases and then reaches a plateau as the defect size increases, which is analogous to the relation between κ_d and $\bar{\delta}$ found in our previous work,¹³ even though the values of the plateaus are different because the geometry of the flat defects is different from the dimple-like defects studied in the previous work. When the steady state is attained (solid circles), the swelling layer on top

shells heal the large defect. The knockdown factor first decreases as the defect size increases and then achieves a minimum value of $\kappa_d = 0.50$ at $\bar{\delta} = 0.33$. The knockdown factor then increases as the imperfection increases further. The minimum value of $\kappa_d = 0.50$ in the steady state is higher than the value of the plateau $\kappa_d = 0.43$ in the initial state. On the other hand, the knockdown factor of the shrinking layer on top shells is nearly constant at first and then decreases as the defect amplitude increases both in the initial (open triangles) and steady (solid triangles) states. The value of the plateau for shells with large defects is lower in the steady state than in the initial state.

Fig. 4(b) shows how the knockdown factor varies from the initial to the steady state. Specifically, we plot the variation of the knockdown factor, $\Delta\kappa_d = \kappa_{d,\text{steady}} - \kappa_{d,\text{initial}}$, versus the normalized defect amplitude, $\bar{\delta}$; a positive value means that the shell was strengthened over time. The shrinking layer on top shells (crosses) have negligible $\Delta\kappa_d$ for small defect sizes, and then decreasing $\Delta\kappa_d$ from +0.10 to -0.19 with $\bar{\delta}$. The swelling layer on top shells (squares) see their $\Delta\kappa_d$ increase from -0.12 to $+0.26$ with the defect size, except when the defect and its thickness at the center are too large ($\bar{\delta} > 0.8$). Overall, differential swelling can increase or decrease the knockdown factor of bilayer shells. Small defects in the swelling layer on top shells are aggravated by differential swelling. However, large defects ($\bar{\delta} > 0.4$) are healed as the knockdown factor increases, by as much as $\Delta\kappa_d = 0.26$. The minimum knockdown factor for the swelling layer on top shells is $\kappa_d = 0.50$. On the other hand, the knockdown factor of the shrinking layer on top shells slightly changes with small defects, and decreases with large defects over time due to differential swelling by $\Delta\kappa_d = -0.19$, at most.

4 Finite element simulations

To help us in better understanding the knockdown factor evolution observed in the experiments and explore a broader parameter space, we conducted simulations using the FEM to model bilayer shells with residual swelling and compute their buckling load under applied pressure. In the simulations, the swelling or shrinking of the two layers is simulated, analogously, by thermal expansion or contraction, respectively. Even though this does not represent a physically-accurate model of swelling, and a microscopically-based swelling model should be used, this simplified approach does take into account the geometric changes (variations in natural curvature) similar to those induced by swelling, as also discussed in previous studies.^{18,31} Note also that, since the swelling changes the shape of the shell just after fabrication, we could not experimentally measure the initial shape of the bilayer shells using X-ray tomography, which is a relatively slow technique (each scan took approximately 1.5 hours). Therefore, in the FEM simulations we used the deformed shape measured in the steady state as the natural configuration, which then undergoes thermal deformation. The thermal expansion and contraction of the two layers are assumed to have the same magnitude.

The induced natural curvature k is described by the curvature of a bilayer strip under differential thermal expansion³² as

$$kh = \frac{48\varepsilon_T}{(14 + E_1/E_2 + E_2/E_1)}, \quad (1)$$

where ε_T is the thermal expansion strain, and E_1 and E_2 are the Young's moduli of the two materials.

We performed FEM simulations using the commercial finite element modeling package ABAQUS/STANDARD. The hemispherical bilayer shell is reduced to a 2D axisymmetric model since the buckling observed in our experiments is axisymmetric. The two layers are modeled by incompressible neo-Hookean materials with the initial Young's moduli measured in experiments. Each layer is discretized by the reduced hybrid axisymmetric elements CAX4RH with a regular mesh of 8 elements in the thickness direction, and 1000 elements in the longitudinal direction. Geometric nonlinearity is considered in the simulations. The shell is clamped at the equator and a temperature field is applied to induce the thermal expansion and contraction in the two layers. The shell deforms to a new configuration under this differential thermal expansion. The magnitude of natural curvature is controlled by the temperature field. We then depressurize the shell by applying a uniform live pressure on its outer surface, for different values of natural curvature. The simulation is conducted using the Riks method, which solves for the equilibrium states by prescribing the arc-length of the load–displacement curve. The buckling pressure is defined as the maximum pressure and is divided by the buckling pressure of a perfect bilayer shell, which is predicted by FEM using eigenvalue buckling analysis, to get the knockdown factor.

4.1 FEM results using the experimentally measured shape of shells

We proceed by taking the deformed geometry of the shell measured in the experiments using X-ray computed tomography and compare FEM predictions with experimental results. As described in Section 2.3, the axisymmetric shape is obtained by averaging the extracted curves along three meridians at different azimuthal angles.

We increase the differential thermal expansion and predict the knockdown factor for different values of natural curvature. Using the time evolution of the natural curvature, experimentally characterized in a bilayer beam (Appendix A, Fig. 7), we plot the knockdown factor as a function of time and compare with the experimental results, as shown in Fig. 5. FEM simulations can qualitatively describe the evolution of the knockdown factor. For the shrinking layer on top shells (Fig. 5(a)), the numerical results agree well with the experiments. The shells weaken with time, except for small defects ($\delta = 0.2$ mm). For the swelling layer on top shells (Fig. 5(b)), the simulations predict the evolution of the knockdown factor only qualitatively. The lack of quantitative agreement may be due to the over-simplification in the modeling of swelling *via* thermal expansion, and to the fact that in numerical simulations, the experimentally measured deformed shape is used as

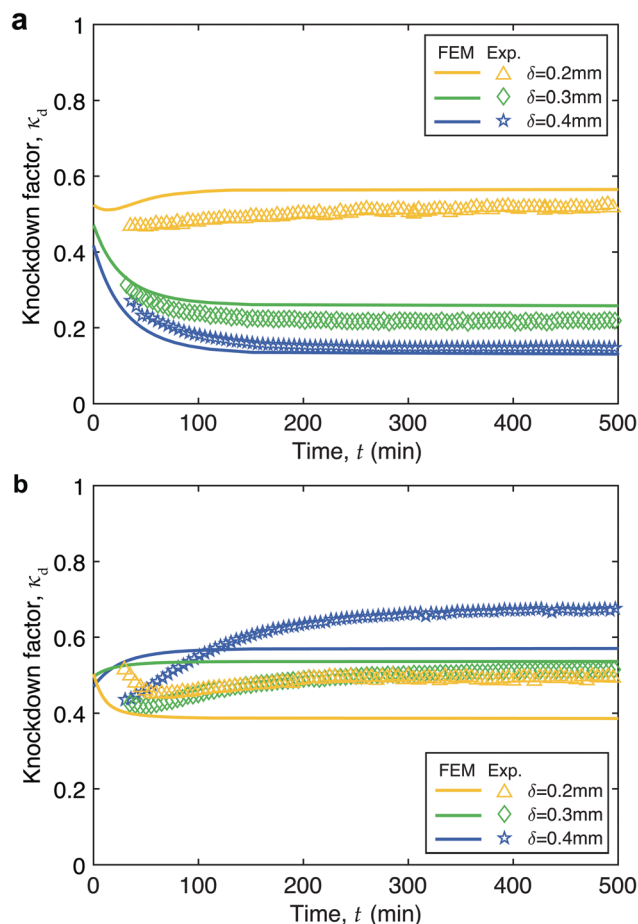


Fig. 5 Evolution of the knockdown factor predicted by FEM simulations, which consider the experimentally measured deformed shapes of the shells, compared with experimental results, for the (a) shrinking layer on top shells and (b) swelling layer on top shells. The amplitude of the flat defect is varied: $\delta = \{0.2, 0.3, 0.4\}$ mm.

the natural configuration, which then undergoes thermal deformation.

Next, we perform a parametric study where a swelling layer on top shell with an engineered defect and a non-homogeneous thickness undergoes differential thermal expansion, toward shedding light on the various parameters at play.

4.2 Influence of thickness variation on the evolution of the knockdown factor

In the numerical exploration of the parameter space that we present next, we describe the normalized shell thickness as

$$\frac{h'}{h} = \begin{cases} 1 + \frac{\delta_h}{h} \cos^2\left(\frac{\theta}{\theta_0}\pi\right), & \frac{1}{2}\theta_0 \leq \theta \leq \frac{3}{2}\theta_0, \\ 1, & \theta < \frac{1}{2}\theta_0 \text{ or } \theta > \frac{3}{2}\theta_0, \end{cases} \quad (2)$$

where δ_h is the amplitude of thickness variation, and θ_0 is the half angular width of the flat defect so that $\cos\theta_0 = 1 - \delta/R$ (Fig. 6(a)). We vary δ_h/h from 0 to 0.5 for shells with different defect amplitudes. In this parametric study, we focus on

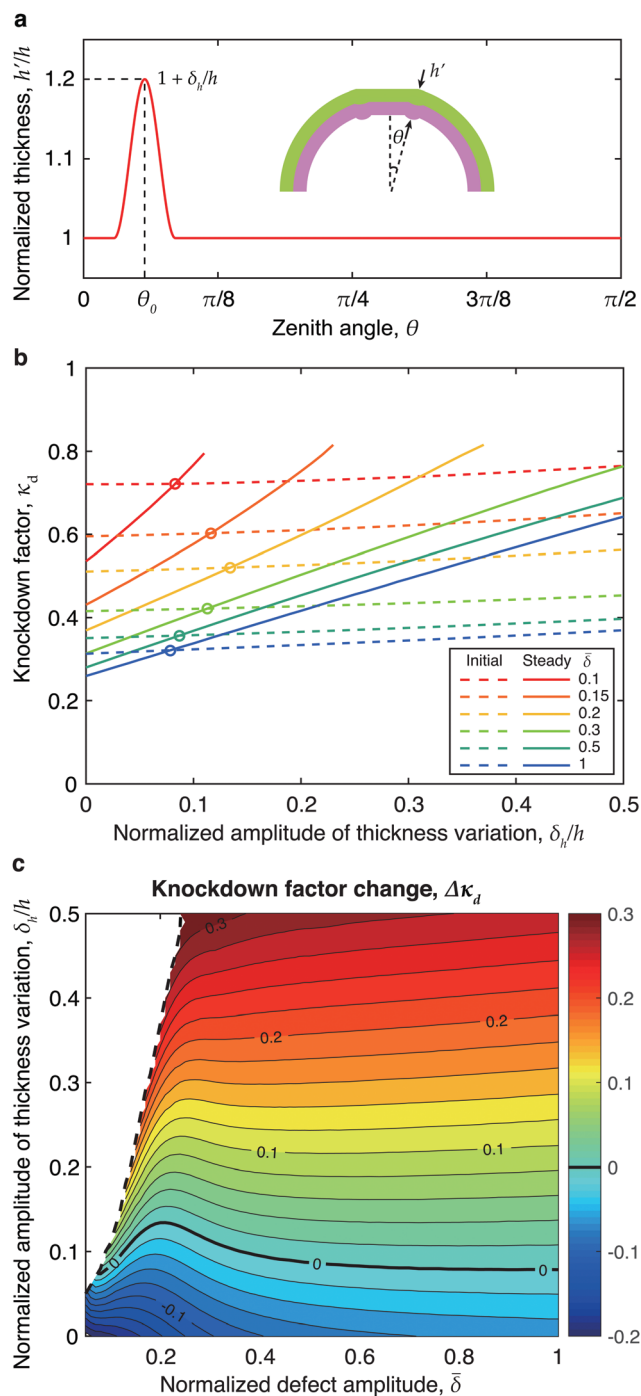


Fig. 6 (a) Thickness profile as a function of the zenith angle θ in FEM simulations ($\delta_h/h = 0.2$ and $\theta_0 = 0.057\pi$). (b) Knockdown factor κ_d versus normalized amplitude of thickness variation δ_h/h , in the initial state (dashed curves) and in the steady state (solid curves), predicted by FEM simulations, for swelling layer on top shells. The normalized defect amplitude is varied as $\bar{\delta} = \{0.1, 0.15, 0.2, 0.3, 0.5, 1\}$. (c) Contour plot of the knockdown factor change $\Delta\kappa_d$ for different values of the normalized amplitude of thickness variation δ_h/h and normalized defect amplitude $\bar{\delta}$.

swelling layer on top shells, as they can exhibit both increasing and decreasing knockdown factors.

Fig. 6(b) shows the knockdown factor for swelling layer on top shells with different thickness variations, in the initial state

($kh = 0$) and in the steady state ($k_{th} < 0$). For a shell with a specific defect amplitude, the change in knockdown factor from the initial state to the steady state is indicated by the distance between the dashed and the solid curves. For shells with a small thickness variation, the knockdown factor decreases due to swelling. For larger thickness variations, the shells strengthen, resulting in a positive change in the knockdown factor. As shells with larger thickness variations manifest larger increases in the knockdown factor, this parametric study suggests that thickness variation is a key parameter in this phenomenon.

Fig. 6(c) shows the contour plot of $\Delta\kappa_d$ for different values of the normalized amplitude of thickness variation δ_h/h and normalized defect amplitude $\bar{\delta}$: the contour line with $\Delta\kappa_d = 0$ (thick solid line in Fig. 6(c)) corresponds to the boundary between the strengthening and weakening of shells due to differential swelling. We observe that for shells with a large defect, $\bar{\delta} > 0.3$, the change in the knockdown factor is much more sensitive to the thickness variation than to the defect amplitude. We notice that in the blank (white) region of the contour map, the shells have a very small defect but a relatively large thickness variation, such that the shell is locally strengthened at the north pole, and buckling occurs at the equator of the shell. This buckling regime is out of the scope of this paper.

5 Conclusions

In closing, we have introduced a minimal mechanism that can be used to modify the buckling pressure, and hence the knockdown factor, of hemispherical bilayer shells, due to differential swelling. The natural curvature of the bilayer system changes due to swelling, which, in turn, induces both a shape change and a build-up of residual stress. Consequently, the critical buckling pressure of bilayer shells with differential swelling is modified with respect to the reference non-swelling case. Depending on the size of the initial defect and the magnitude of swelling, shells can strengthen or weaken against buckling.

An experimental fabrication method was developed to produce hemispherical bilayer shells that contain a single flat defect at their pole, the amplitude of which was varied systematically. The critical pressure for the onset of buckling for these shells was measured while polymer chains were diffusing across the bilayer interface, causing differential swelling. The experimental results show that swelling layer on top shells have a higher knockdown factor than shrinking layer on top shells. Moreover, we found that the knockdown factor of swelling layer on top shells could increase over time due to differential swelling, depending on the size of the defect. This healing of imperfections is more effective when the initial amplitude of the defect is large. In parallel to the experiments, we carried out FEM simulations to further explore the underlying mechanism and found a qualitative agreement with experiments. The FEM indicates that the change of shape had a primary role in increasing and decreasing the knockdown factor during differential swelling. Spatial variations of the shell thickness

significantly were also found to be particularly important in affecting the time evolution of the knockdown factor or shape-changing shells.

We believe that the mechanism that we have introduced and investigated to evolve the knockdown factor of spherical bilayer shells over time could be extended to bimetallic shells or shells made of pH-responsive gels to dynamically control their buckling conditions. In addition, since the mechanical response of the shells is dependent on both the timescale and magnitude of residual swelling, these results suggest that a more detailed characterization of the residual solvent and the physics of residual swelling is necessary in the future.

Conflicts of interest

There are no conflicts to declare.

Appendix A: Characterization of a bilayer beam undergoing differential swelling

Differential swelling causes a change in the natural curvature of a thin structure. One-dimensional objects, like beams that are either flat or initially curved, can simply bend to accommodate this change in curvature. On the other hand, plates and shells cannot simply bend and accumulate residual stress that can eventually lead to instabilities. Hence, to relate the diffusion of free chains to the natural curvature, it is important to quantify how beams deform, since they have no geometric incompatibilities that can lead to instability. Therefore, in this Appendix, we investigate the mechanics of deformation of rectangular bilayer films that are originally flat, with an emphasis on quantifying the evolution of their natural curvature as a result of differential swelling, and measuring their mechanical properties.

We have performed a series of experiments to characterize the natural curvature, the bending stiffness, and the axial stiffness of a bilayer beam. We define the natural curvature of a beam as its curvature in the absence of external loads (e.g., gravity), which can be measured as the curvature of the beam bending set orthogonally to the gravitational field (see Fig. 7(a)). Then, if the same beam bends under gravity (Fig. 7(b)), its shape will be the result of the combined effects of natural curvature and bending stiffness. Assuming that the former has already been quantified, the latter can be determined as a function of time. Furthermore, the effective axial tensile stiffness can be measured with an independent tension test.

An initially flat bilayer film was fabricated using the following protocol. First, VPS-32 was mixed with a base/cure ratio of 1:1 in weight and the liquid solution was coated onto a glass plate using an automatic film applicator (ZAA2300, Zehntner GmbH Testing Instruments), which, upon curing, yielded a solid sheet of thickness $h_1 = 0.3$ mm. Second, a liquid suspension of VPS-8 was mixed (also with a base/cure ratio of 1:1 in weight) and poured onto the previously cured VPS-32 film, and

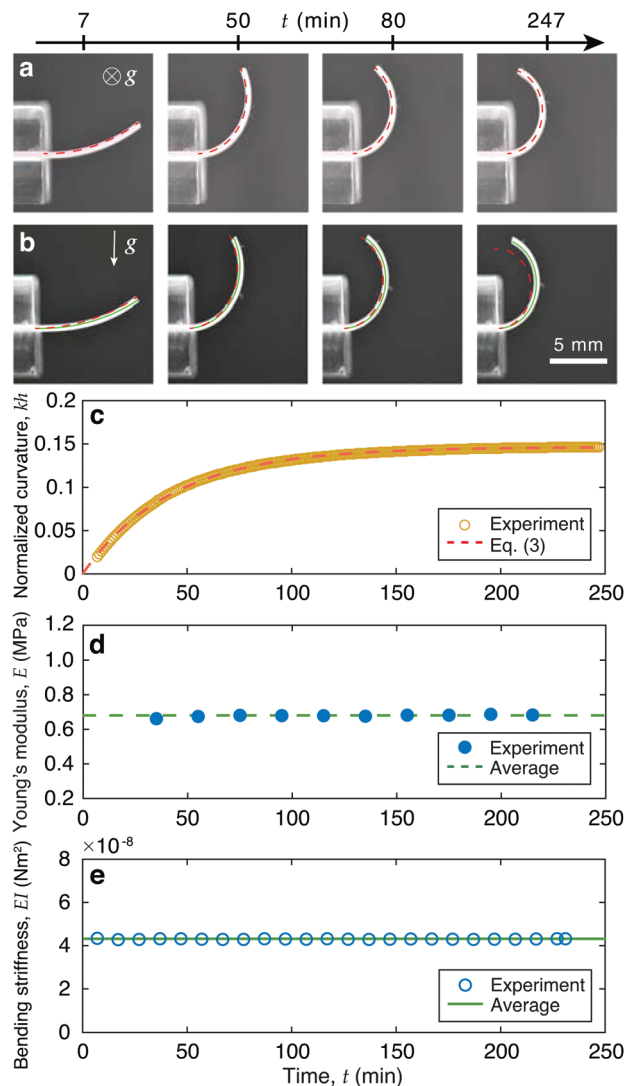


Fig. 7 (a and b) Photographs of a bilayer beam with thickness $h = 0.6$ mm, deforming (a) orthogonally and (b) against gravity. The dashed line corresponds to the fitted circle and the solid line is the solution of eqn (4) with the determined bending stiffness. (c) Time evolution of the natural curvature of the bilayer beam, $k(t)$. The dashed line corresponds to the fit of eqn (3). (d) Young's modulus, E , and (e) bending stiffness, EI , of a bilayer beam as a function of time. The lines correspond to the average values. The error bars are smaller than the symbol size.

cured, achieving the same thickness of $h_2 = h_1$, set by the film applicator. Note that these specific values for h_1 and h_2 were chosen because they are also the values for the targeted thicknesses of the bilayer shells used in this manuscript, whose fabrication procedure is described in Section 2.1. Upon curing of the VPS-8 film ($\tau_c = 10$ min measured from the end of mixing), we set a timer and then cut a rectangular strip from the bilayer film with a thickness $h = h_1 + h_2 = 0.6$ mm, width $w = 2$ mm, and length $l = 12$ mm. To measure the natural curvature, this bilayer strip was clamped as depicted in Fig. 7(a), such that the bending deformation occurred orthogonally to gravity, and time-lapsed photographs were taken (Nikon 850).

From the digital photographs, we fit a circle of radius R to the mid-surface of a bilayer beam (red dashed lines in Fig. 7(a)). We define the curvature of the bilayer beam as $k(t) = 1/R$, which is time-dependent due to the differential swelling. In Fig. 7(c), we plot the normalized curvature kh of the bilayer beam as a function of time, t . We find that the experimental data (circles) are well described by

$$kh = k_f h (1 - e^{-t/T}), \quad (3)$$

where k_f is the final curvature once the steady state has been reached, and T is the characteristic time constant associated with the diffusive process across the interface of the bilayer. For this particular sample, the final normalized curvature was measured to be $k_f h = 0.1462 \pm 0.0016$, and the characteristic time was $T = 42.5 \pm 0.2$ min by curve fitting (the \pm values correspond to the 95% confidence bounds). The latter represents the ratio between the square of the characteristic length (in this case the thickness of the shell) and the diffusivity of the bilayer system. These results indicate that the diffusion time scale is significantly larger than the curing time scale of the VPS polymers ($\tau_c \approx 10$ min for both VPS-8 and VPS-32). As discussed in Section 2, where we characterize the response of bilayer shells (e.g., shape and buckling pressure) during swelling, the time intervals chosen for data acquisition ($\Delta t = 5$ min) provide sufficiently dense data to represent the time evolution of the process.

In addition to the evolution of the natural curvature of the bilayer beams reported above, we have also measured the time-dependence of their mechanical properties. The Young's moduli of VPS-32 and 8 were measured to be $E_1 = 1.164 \pm 0.026$ MPa and $E_2 = 0.267 \pm 0.002$ MPa, respectively. The effective Young's modulus, E , of the bilayer beam was measured through tensile tests (Instron 5943 mechanical testing system with a 5 N load cell). For this purpose, we fabricated a dog-bone shaped bilayer specimen with a length (reduced parallel section) of $l = 100$ mm, width $w = 12.15$ mm, and thickness $h = h_1 + h_2 = 0.6$ mm. The measurements were repeated every 20 min to detect any possibility of time-dependence due to differential swelling and the results are plotted in Fig. 7(d). Then, we measured the bending stiffness, EI , of the bilayer beam, for which we positioned the bilayer beam as shown in Fig. 7(b), so as to have the beam bending against gravity. The elastica equation with gravity and natural curvature was solved numerically, and the value of EI was determined so as to minimize the quadratic distance between the numerical solution and the experimental profile of the beam deforming with the effect of gravity. The elastica description we used, in terms of dimensionless quantities, is given by³³

$$\theta''(s) - \frac{1-s}{\beta} \cos \theta(s) = 0, \quad (4)$$

where θ is the angle of the tangent vector of the neutral axis of the beam with respect to the horizontal axis, s is the dimensionless arc-length nondimensionalized by the total length of the elastica L , and β is a dimensionless parameter defined as $\beta = EI/(\rho g S L^3)$, where ρ is the density, and S is the cross-sectional area. Without gravity (configuration in Fig. 7(a)), β becomes infinite, such that the

associated term in eqn (4) vanishes, and the solution of the equation is a segment of a circle. Under gravity (configuration in Fig. 7(b)), we determine the value of β that best fits the experimental profile, which in turn yields the value of EI . The natural curvature, which is homogeneous along s , enters the problem *via* a boundary condition at the free end, equivalent to an applied torque: $\theta'(1) = Lk$. In Fig. 7(e), we plot the time evolution of the experimentally determined bending stiffness, EI , of the bilayer beam, obtained using the fitting procedure mentioned above. From the ensemble of the results in Fig. 7, we found that both $E = 0.68 \pm 0.02$ MPa and $EI = 4.31 \pm 0.03 \times 10^{-8}$ Nm² are constant to within 3% (MAD) over time.

Appendix B: Fabrication of PDMS molds

To manufacture our hemispherical bilayer shell samples, we first fabricated thick elastic shells out of PDMS, which were used as molds to produce our desired VPS-8/VPS-32 bilayer shells using a coating technique. To make these PDMS molds, we first machined stainless steel bearing balls (TIS Wälzkörpertechnologie GmbH) that were originally spherical, with a radius of 25.4 mm, to flatten their pole with a set amplitude in the range $0 \leq \delta$ [mm] ≤ 0.5 . Second, we poured a PDMS mixture onto the machined stainless balls with a waiting time $\tau_w \approx 30$ min between the preparation of the mixture and the moment of pouring to tune the viscosity.¹² The PDMS base, curing agent (Sylgard 184, Dow Corning), and cure accelerator (3-6559 Cure Accelerator, Dow Corning) were previously mixed in a 10 : 1 : 2 weight ratio.

These PDMS molds were cured in a convection oven at 40 °C. We repeated pouring and curing of PDMS six times to obtain hemispherical molds with the desired thickness of $h_{\text{mold}} = 2.0 \pm 0.1$ mm. Upon curing, the molds were sufficiently thick and stiff so as to not deform from the target shape under self-weight. Finally, the thick PDMS shells were peeled from the stainless spheres and the resulting molds had an inner radius of 25.4 mm and a single flat defect at their pole with amplitude δ , which was varied systematically.

Acknowledgements

We thank Joel Marthelot (Aix-Marseille University) and Francisco López-Jiménez (University of Colorado Boulder) for useful discussions and interactions in the earlier stages of this work. DPH and PMR gratefully acknowledge the financial support from NSF through the independent grants CMMI-1824882 and CMMI-1351449 (CAREER), respectively.

References

- 1 R. Zoelly, PhD thesis, ETH Zürich, Zürich, Switzerland, 1915.
- 2 W. T. Koiter, *Proc. K. Ned. Akad. Wet.*, 1969, **B72**, 40–123.
- 3 J. W. Hutchinson, *J. Appl. Mech.*, 1967, **34**, 49–55.

- 4 Y. Forterre, J. M. Skotheim, J. Dumais and L. Mahadevan, *Nature*, 2005, **433**, 421–425.
- 5 E. Katifori, S. Alben, E. Cerda, D. R. Nelson and D. Jacques, *Proc. Natl. Acad. Sci. U. S. A.*, 2010, **107**, 7635–7639.
- 6 H. W. Gerald Lim, M. Wortis and R. Mukhopadhyay, *Proc. Natl. Acad. Sci. U. S. A.*, 2002, **99**, 16766–16769.
- 7 S. Sacanna, W. Irvine, P. Chaikin and D. Pine, *Nature*, 2010, **464**, 575–578.
- 8 R. L. Carlson, R. L. Sendelbeck and N. J. Hoff, *Exp. Mech.*, 1967, **7**, 281–288.
- 9 R. H. Homewood, A. C. Brine and A. E. Johnson, *Exp. Mech.*, 1961, **1**, 88–96.
- 10 I. Elishakoff, *Resolution of the Twentieth Century Conundrum in Elastic Stability*, World Scientific Publishing, Singapore, 2014.
- 11 P. Seide, V. I. Weingarten and E. J. Morgan, Final Report: STL/TR-60-0000-19425, Space Technology Laboratories, Inc., Los Angeles, CA, 1960.
- 12 A. Lee, P.-T. Brun, J. Marthelot, G. Balestra, F. Gallaire and P. Reis, *Nat. Commun.*, 2016, **7**, 11155.
- 13 A. Lee, F. López Jiménez, J. Marthelot, J. W. Hutchinson and P. M. Reis, *J. Appl. Mech.*, 2016, **83**, 111005.
- 14 A. Djellouli, P. Marmottant, H. Djeridi, C. Quilliet and G. Coupier, *Phys. Rev. Lett.*, 2017, **119**, 224501.
- 15 R. R. Meyer and R. J. Bellingante, Fabrication and experimental evaluation of common domes having waffle-like stiffening, Missile & Space Systems Division Douglas Aircraft Company, Inc. Technical Report Douglas Report SM-47742, 1964.
- 16 P. S. Song and S. Hwang, *Constr. Build. Mater.*, 2004, **18**, 669–673.
- 17 L. M. C. Sagis, R. de Ruiter, F. J. R. Miranda, J. de Ruiter, K. Schroën, A. C. van Aelst, H. Kieft, R. Boom and E. van der Linden, *Langmuir*, 2008, **24**, 1608–1612.
- 18 M. Pezzulla, N. Stoop, M. P. Steranka, A. J. Bade and D. P. Holmes, *Phys. Rev. Lett.*, 2018, **120**, 048002.
- 19 M. Pezzulla, G. P. Smith, P. Nardinocchi and D. P. Holmes, *Soft Matter*, 2016, **12**, 4435–4442.
- 20 D. V. Panov, *J. Appl. Math. Mech.*, 1947, **11**, 603–610.
- 21 W. H. Wittrick, D. M. Myers and W. R. Blunden, *Q. J. Mech. Appl. Math.*, 1953, **6**, 15–31.
- 22 S. P. Timoshenko and J. M. Gere, *Theory of Elastic Stability*, McGraw-Hill, 1961.
- 23 B. D. Aggarwala and E. Saibel, *Int. J. Non Linear Mech.*, 1970, **5**, 49–62.
- 24 L. Ren-Huai, *Int. J. Non Linear Mech.*, 1983, **18**, 409–429.
- 25 S. E. Rutgerson and W. J. Bottega, *Int. J. Solids Struct.*, 2002, **39**, 4867–4887.
- 26 M. Pezzulla, S. A. Shillig, P. Nardinocchi and D. P. Holmes, *Soft Matter*, 2015, **11**, 5812–5820.
- 27 E. Ventsel and T. Krauthammer, *Thin Plates and Shells: Theory, Analysis, and Applications*, CRC Press, 2001.
- 28 D. Sharp, *Phys. D*, 1984, **12**, 3–18.
- 29 C. Pozrikidis, *J. Fluid Mech.*, 1988, **188**, 275–300.
- 30 M. Vlachogiannis and V. Bontozoglou, *J. Fluid Mech.*, 2002, **457**, 133–156.
- 31 E. Efrati, E. Sharon and R. Kupferman, *J. Mech. Phys. Solids*, 2009, **57**, 762–775.
- 32 S. P. Timoshenko, *J. Opt. Soc. Am.*, 1925, **11**, 233–255.
- 33 B. Audoly and Y. Pomeau, *Elasticity and geometry: from hair curls to the non-linear response of shells*, Oxford University Press, 2010.